Understanding the role of Al doping of LiCoO2 on the mechanisms upon cycling up to high voltages (≥4.6 V vs Li+/Li)

Fatima-Ezzahra Er-Rami, Marie Duffiet, Sean Hinkle, Jérémie Auvergniot, Maxime Blangero, Pierre-Etienne Cabelguen, Kyeongse Song, François Weill, Claude Delmas, Dany Carlier

Understanding the role of Al doping of $LiCoO_2$ on the mechanisms upon cycling up to high voltages (≥ 4.6V vs. Li^+/Li)

Fatima-Ezzahra Er-Rami [a,b], Marie Duffiet [a,b], Sean Hinkle [a], Jérémie Auvergniot [b] Maxime Blangero[c], Pierre-Etienne Cabelguen [b], KyeongSe Song [c], François Weill [a], Claude Delmas [a], Dany Carlier [a*]

[a] Univ. Bordeaux, CNRS, Bordeaux INP, ICMCB, UMR 5026, F-33600 Pessac, France

[b] Umicore Rechargeable battery materials, 31 rue du marais, Brussels BE-1000, Belgium

[c] Umicore, Materials Research and Development, Cheonan-Shi, Chungnam-Do 330-200, Korea

* Corresponding author: dany.carlier@icmcb.cnrs.fr

Abstract

The effect of Al doping on the structure and electrochemical properties of $LiCoO_2$ was investigated for a 4% doping amount, of practical interest for industrial application. Characterization of materials with low doping amount and precise control of its overall stoichiometry and homogeneity is challenging, and could be performed in this study combining ^{7}Li, ^{27}Al, ^{59}Co Nuclear Magnetic Resonance (NMR) and X-Ray Diffraction (XRD). ^{27}Al MAS NMR and XRD studies revealed that the Al-doping is homogeneous, and ^{7}Li MAS NMR indicates that its stoichiometry (Li/M=1.00) is ideal. The electrochemical tests have shown that Al doping improves the cycling stability at 4.6V and strongly impacts the voltage curve profile up to 5V. By an ex-situ XRD study of electrochemically deintercalated $Li_xCo_{0.96}Al_{0.04}O_2$ and Li_xCoO_2 materials controlling the state of charge or the voltage, we showed that Al doping delays the formation of the H1-3 and O1 phases. Our ^{7}Li MAS NMR and TEM results revealed the formation a lithiated spinel-type phase at the surface of the Al-doped electrode material, together with the formation of a stable CEI layer unlike for $LiCoO_2$. The different nature of the electrode/electrolyte interphases may therefore explain to better ionic/electronic conductivities of the Al-doped electrode and may hinder the Co dissolution at high voltage.

1. Introduction

O3-$LiCoO_2$ was first proposed as positive electrode material for lithium-ion batteries (LIBs) by Goodenough et al. in1980.[1] It is still widely used as positive electrode material in commercialized LIBs for portable electronics devices. Indeed, the main advantages are: a relatively large theoretical specific capacity as high as 274 mAh/g and an electrode density close to $4.0 g/cm^3$ resulting in high practicable energy density and an excellent cycle stability.[2] Layered $LiCoO_2$ synthesized at high temperature exhibits the α-$NaFeO_2$ type structure[3] (R-3m space group with $a_{hex.}$= 2.816 Å; $c_{hex.}$ = 14.052 Å) with an O3 stacking according to the nomenclature developed by Delmas et al.[5] Considerable efforts have been carried out to understand the structural changes occurring during electrochemical cycling by X-Ray diffraction and first principles calculations many years ago.[4,7,8] When Li is deintercalated from $LiCoO_2$, the material undergoes a series of phase transitions; the first occurs at a characteristic voltage plateau of ~3.9V versus Li^+/Li

($0.75 \leq x \leq 0.94$ in Li_xCoO_2). It corresponds to a two-phase region induced by an insulator–metal transition where a newly appeared rhombohedral phase (called $O3_2$) coexists with the pristine $LiCoO_2$ ($O3_1$).[8] More recently, the composition domain of the plateau has been revisited for a "real" stoichiometric $LiCoO_2$: only when absolutely no structural defects are present, the two-phase domain starts quite at the onset of Li deintercalation.[10] Then, when ~ 0.5 Li is deintercalated, the system undergoes a transition from rhombohedral O3 to monoclinic O'3[6] due to a lithium/vacancy in-plane ordering.[4,5,11] Li deintercalation in $LiCoO_2$ is highly reversible when the cell is cycled up to 4.2 V vs Li^+/Li explaining its excellent cyclability when used as positive electrode material in LiBs with a specific capacity of 137 mAh/g vs Li^+/Li. In order to achieve a higher capacity and increase the energy density, cycling voltage above 4.3 V vs Li^+/Li is required. However, working at high voltage leads to a deterioration of the cycling performances,[12] caused by structural instabilities, electrolyte degradation and Co dissolution.[13–18] More specifically, for charge voltages exceeding 4.5 V, $LiCoO_2$ exhibits detrimental phase transformations: O3 to H1-3 and H1-3 to O1 implying slab glidings.[8,14,19] Consequently, internal strain builds up, leading to crack formation and particle pulverization.[15,20,21] Several strategies were investigated to improve the cycling stability of $LiCoO_2$.[22–24] Among these, metal substitutions of cobalt (Al, Mg, Ti…) have been demonstrated to be a promising and effective method to enhance the electrochemical performances of $LiCoO_2$ at high voltage.[2,25–28] In 1998, Ceder et al.[29] identified aluminum as a potentially attractive dopant: they observed that substituting Co with Al leads to a higher Li cell average voltage but suffers from a lower capacity at the first charge up 4.4V vs Li^+/Li.[29,30] The similar Al^{3+} and LS-Co^{3+} ionic radii (0.535 Å vs. 0.545 Å) facilitate the substitution while maintaining the layered structure. It has been also reported that the substitution of Co by Al was effective on suppressing cobalt dissolution at 4.5 V versus Li^+/Li.[31] In these previous works, the authors speculate that the dopant element is homogeneously distributed within the Co sites. Here, the challenge is to characterize both the Al repartition and the deintercalation mechanisms in an Al doped-$LiCoO_2$ sample with a low dopant concentration at a level of industrial relevance (4%).

Previous studies have shown that ^7Li Magic Angle Spinning Nuclear Magnetic Resonance (MAS NMR) is a key tool to discuss the Li/M stoichiometry[32,33] whereas ^{27}Al and ^{59}Co MAS NMR can be used to characterize the Al/Co distribution homogeneity in the slab, even with a low doping level.[34,35] Several 4% Al-doped $LiCoO_2$ materials with controlled Li/(Co + Al) stoichiometries synthesized by various solid state routes have been recently studied in our group.[34,36] Using ^7Li,

^{27}Al ,^{59}Co MAS NMR and synchrotron X-Ray Diffraction (XRD) the exact Li/M stoichiometry and their doping homogeneity were discussed. The materials were compared with a $LiCo_{0.96}Al_{0.04}O_2$ sample prepared by co-precipitation that also exhibits homogeneous Al/Co repartition, but lower particles size. For extensive cycling at high voltage, the sample prepared by the solid-state route showed, however, better stability, since larger particles size minimizes the electrolyte degradation's detrimental effect. Therefore, a sample prepared by a solid state route with homogeneous Al/Co distribution and a Li/M ratio equal to 1.00 has been selected for the present study. In a first part, we report the structural characterizations of the 4% Al-doped $LiCoO_2$ discussing its homogeneity. Then, we aim to understand the role of Al-doping on the high voltage degradation mechanisms involved during cycling, combining techniques with different spatial and sensitivity scales such as XRD, ^{7}Li, ^{59}Co, and ^{27}Al MAS NMR and TEM.

2. Materials and methods:

4% Al-doped $LiCoO_2$ sample was synthesized in Umicore R&D center by a solid state route from a mixture of Al_2O_3, Co_3O_4 and Li_2CO_3 as described in more details in our previous work.[34] The de-intercalated $Li_xCo_{0.96}Al_{0.04}O_2$ ($x<1$) samples were later prepared by electrochemical deintercalation in Li cells following the procedure disclosed in the next paragraph of this experimental section. A reference material, stoichiometric $LiCoO_2$ (st-$LiCoO_2$) with an exact Li/Co = 1.00 stoichiometry has been also synthesized by a solid state route. In order to avoid the formation a slightly overlithiated compound, as overlithiation impacts the cycling properties of $LiCoO_2$, a blend nominal Li/Co=0.98 ratio was used, and the precursors were heat treated at 1050°C for 12h. In such thermodynamic synthesis conditions, the reaction products are expected to be st-$LiCoO_2$ with traces of Co_3O_4 impurity as will be discussed in the following. Subsequently, grinding and annealing at 800 ° C for 5 hours was carried out in order to ensure good homogeneity of the materials and ensure representative and consistent analytical assessment. Final experimental (Li/Co) and (Li/(Al+Co)) ratios obtained by Induced Coupled Plasma (ICP) for st-$LiCoO_2$ and $LiCo_{0.96}Al_{0.04}O_2$ materials are gathered in **Table 1**. The results show that the experimental values are in good agreements with the theoretical ones.

Target compounds	Li/Co		Li/M (M=Co+Al)	
	Target	Experimental	Target	Experimental
St-$LiCoO_2$ (+Co_3O_4)	0.98	0.971	-	-
$Li_{1.00}Co_{0.96}Al_{0.04}O_2$	1.04	1.039	1.00	0.998

Table 1: ICP analysis of the $LiMO_2$ samples prepared using Li/Co = 0.98 and Li/M = 1.00 with M = 96% Co + 4% Al.

Electrodes of undoped and 4%Al-doped $LiCoO_2$ were prepared by mixing 90% weight of active material, 5% of carbon black, and 5% of polyvinylidene fluoride (PVDF). A slurry was formed by adding N-methyl-pyrrolidone (NMP) and mixed for 1h. The slurry casted onto a 30 µm-thick-aluminum foil, was dried in an oven for 2 hours at T = 80 °C, calendared and punched into discs with an electrode density of ~3.0g/cm^3. The electrodes were then dried overnight under vacuum at T = 120 °C and stored in an argon-filled glovebox, where cell assembling was carried out. Electrochemical tests were both carried out in coin cells and Swagelok type cells. Coin cells were used to assess the electrochemical performance of all samples (ie, charge and discharge capacities, cycle life performance, etc…), while the Swagelok-type design was favored when the cycled samples needed to be recovered for further characterization. Two different loading of the electrodes were used depending on the cell setup. The coin cells were assembled using $LiCo_{0.96}Al_{0.04}O_2$ or st-$LiCoO_2$ positive electrodes with a 10 mg/cm^2 active material loading, a disc of Viledon® and Celgard 2400® as separators and a Li metal sheet as negative electrode with 1 M $LiPF_6$ in EC: DEC: DMC as electrolyte. A higher loading of ~ 30 mg/cm^2 was employed to prepare Li de-intercalated $Li_xCo_{0.96}Al_{0.04}O_2$ or Li_xCoO_2 materials in the Swagelok setup to have a sufficient amount of powder for all ex-situ characterizations. One more Viledon separator was added in this case. The materials were recovered in an argon-filled dry box, washed with dimethyl carbonate (DMC) to remove residual electrolyte salt and dried under vacuum. Deintercalated $Li_xCo_{0.96}Al_{0.04}O_2$ and Li_xCoO_2 samples were prepared by two different routes. Route 1: a galvanostatic charge at a C/20 rate applied up to the desired Li content (x) followed by a relaxation step; Route 2: a galvanostatic charge at a C/20 rate applied up to the desired voltage followed by a floating step until the current reached ~ 0 mA. This second procedure was used to prepare

homogeneous samples stable at high voltage. All sample powders of the deintercalated compounds were then split in two parts for NMR and XRD characterization.

Powder X-ray diffraction (PXRD) patterns were collected on a PANalitycal X'pert PRO MPD, diffractometer in Bragg-Brentano θ-θ geometry equipped with a Fe filter, a spinner and X'Celerator multi-strip detector using the Co-$K_{\alpha.}$ Radiations. Each pattern was recorded in the (10 - 120°) 2θ range using 0.016° intervals and 15 h total counting time. XRD patterns of the deintercalated materials were collected on a PANalitycal X'pert[3] Powder diffractometer using the Cu-$K_{\alpha.}$ radiations, that allows the study of powder packed in 0.3 mm diameter capillaries.

NMR experiments were performed using a standard Bruker 2.5 mm MAS probe with a 30 kHz typical spinning frequency. ^{7}Li MAS NMR spectra were recorded on a Bruker 300 Advance spectrometer at 116.66 MHz (7.05 T magnet). A Hahn echo sequence [$t_{\pi/2}$-τ1-t_{π}-τ2] synchronized with one period of rotor rotation was used for a 30 kHz spinning frequency. The 90° pulse duration was equal to $t_{\pi/2}$ = 2.0 μs and determined using a LiCl 1 M solution. A recycle time of D_0 = 40s was used for st-$LiCoO_2$ and $LiCo_{0.96}Al_{0.04}O_2$ samples, whereas a shorter D_0 = 4s was enough for all deintercalated samples, to avoid T_1 saturation effects. Single pulse ^{27}Al MAS NMR spectra were recorded on a Bruker 500 MHz spectrometer at 130.33 MHz (11.7 T magnet). The spectral width was set to 0.5 MHz and the recycle time to D_0 = 5 s, long enough to avoid T_1 saturation effects. As ^{27}Al is a strong quadrupolar nucleus with I = 5/2, a short pulse length of 1.1 μs corresponding to a π/12 pulse determined using an aqueous 1 M $Al(NO_3)_3$ solution was employed. In these conditions, all of the -½ → +½ central transitions are equally excited regardless of the magnitude of the nuclear quadrupole coupling constants and one can extract quantitative data. As all samples contain only 4% of Al, overnight experiments (10240 scans) were carried out to ensure a good signal/noise ratio.

^{59}Co MAS NMR spectra were recorded on a Bruker 500 MHz spectrometer at 120.35 MHz (11.7 T magnet). The spectral width was set to 0.5 MHz and the recycle time to D_0 = 1 s. A single pulse sequence using a short pulse length of 1.1 μs corresponding to a π/16 pulse was used to extract quantitative data. However, it requires a first-order phasing process with a sin x/x baseline correction due to the dead time of the spectrometer not easily determined due to large overlapping signals. The external reference was a 1M $K_3Co(CN)_6$ aqueous solution.

Electron diffraction patterns as well as images of the samples were obtained using a JEOL 2100 transmission electron microscope working at an accelerating voltage of 200kV. Prior to their introduction in the microscope, samples were de-agglomerated in a mortar with addition of DMC, then a few drops of the resulting suspension were deposited on a copper grid with a formvar carbon film.

3. Results and discussion

3.1. Structural properties of pristine st-$LiCoO_2$ and $LiCo_{0.96}Al_{0.04}O_2$ materials

X-ray diffraction patterns of pristine st-$LiCoO_2$ and $LiCo_{0.96}Al_{0.04}O_2$ samples are plotted in **Figure S1**. The two materials exhibit similar line-width and diffraction lines indexed in the rhombohedral R-3m space group of the O3 stacking. Note that the presence of Co_3O_4 as impurity in st-$LiCoO_2$ is in good agreement with the Li/Co=0.98 ratio used for the synthesis and confirm the successful preparation of st-$LiCoO_2$ (with no Li in the Co-layer, further confirmed by NMR below). No asymmetry of the peaks is seen by XRD suggesting a homogeneous Al doping.[34] As Co is partially substituted by Al, the $a_{hex.}$ lattice parameter reflecting the M-M bond length slightly decreases from 2.816 (1) Å to 2.814 (1) (even though the difference is very small it goes with the tendency expected from ionic radii : $r_{Al^{3+}}$= 0.535 Å, $r_{Co^{3+}}$= 0.545 Å). The $c_{hex.}$ lattice parameter related to the interlayer distance, increases more significantly from 14.052 (1) Å to 14.062 (1) Å in agreement with the literature.[30]

$LiCo_{0.96}Al_{0.04}O_2$ and st-$LiCoO_2$ materials exhibit both a single ^{7}Li MAS NMR signal very close to 0 ppm (**Figure S2a**) that indicates that no paramagnetic ions are present in the Li environment,[10] in good agreement with the target formulas. Indeed, for Li/M = 1.00, only diamagnetic LS-Co^{3+} ions with the $t_{2g}^6e_g^0$ electronic configuration are expected in the layered phase. Note that the signal of $LiCo_{0.96}Al_{0.04}O_2$ is slightly broader than the one of st-$LiCoO_2$, as several Li environments versus Co/Al are expected in that material. However, the resolution of the ^{7}Li MAS NMR experiment is too low to distinguish clearly the different contributions. ^{27}Al and ^{59}Co MAS NMR were additionally used to characterize the Al/Co local environments (**Figure S2b** and **S2c**). As discussed in previous works,[34,37] a set of signals is observed, each corresponding to a different Al environment denoted as Al-(Al_nCo_{6-n}) for Al surrounded by n Al^{3+} and (6-n) Co^{3+}. The signal with the higher

chemical shift located at ~62 ppm corresponds to Al surrounded by 6 Co in the slab (denoted as Al-(Al_0Co_6)). This signal exhibits a clear second order quadrupolar line shape. The other signals located at 55 ppm, and 48 ppm correspond to Al surrounded by n Al^{3+} and (6-n) Co^{3+} with n=1 and 2, respectively. Signals for Al in a Al-rich environment with n ≥ 3, expected at lower ppm value[32] were not detected in our sample due to the very low intensity predicted for those environments if Al distribution is homogeneous. Indeed, the relative intensities observed in our sample are really close from the one expected for a statistical repartition of Co and Al in the slab (See **Figure S3**). ^{59}Co MAS NMR spectra of $LiCo_{0.96}Al_{0.04}O_2$ and st-$LiCoO_2$ materials are displayed in **Figure S2c**. St-$LiCoO_2$ exhibits a single signal located at 14137 ppm as expected for LS-Co^{3+} surrounded by 6 LS-Co^{3+} in the slab, in agreement with literature[38]. Despite broader signals observed for ^{59}Co MAS NMR, compared to ^{27}Al MAS NMR, distinct signals can be resolved for $LiCo_{0.96}Al_{0.04}O_2$. The most intense one located at 14132 ppm is assigned to LS-Co^{3+} ions surrounded by six other LS-Co^{3+}, denoted as Co-(Co_6Al_0). The other signals located at 14105 ppm, 14077 ppm, 14047 ppm, and 14021 ppm are assigned to Co surrounded by n Al^{3+} and (6-n) Co^{3+} in the slab with n varying respectively from 1 to 4, denoted as Co-($Co_{6-n}Al_n$).[34] Comparison with statistical intensities was less straightforward due to the strong overlap of those broad signals, but no Al-rich environments (n = 5 and n = 6) were detected.

The deep characterization of the $LiCo_{0.96}Al_{0.04}O_2$ sample (XRD combined to ^{7}Li, ^{27}Al and ^{59}Co MAS NMR) indicates that the sample is diamagnetic, therefore with no Li excess, and that the Al repartition in the Co layer is homogeneous.

3.2. Electrochemical properties and general overview

$LiCo_{0.96}Al_{0.04}O_2$ and st-$LiCoO_2$ were used as positive electrode in Li cells that were cycled at C/20 rate. The resulting cycling curves clearly show that the substitution of Co by a small amount of Al (4%) has a profound effect on the electrochemical behavior (**Figure 1 and 2**).

When st-$LiCoO_2$ is delithiated, several phase transitions occur as discussed in the introduction and reported in **Figure S4**. During the 1st cycling curve of $LiCo_{0.96}Al_{0.04}O_2$ at C/20, a voltage plateau is observed in the low voltage region, but seems less extended that the one related to the Mott insulator-metal transition[9] observed for st-$LiCoO_2$ (**Figure 1**). The cycling curve of

$LiCo_{0.96}Al_{0.04}O_2$ also does not feature the monoclinic transition around x = 0.5 [4,5,11] nor the O3/H1-3 voltage plateau on charge. Another striking difference between the two cycling curves is the large polarization observed at the beginning of the discharge for st-$LiCoO_2$, not present for the doped material. Overall, the Al-doped sample shows a larger irreversible capacity than st-$LiCoO_2$ as previously discussed in the literature.[31,33,35,36]

The suppression of Li/vacancy ordering for x = 0.5, as Co^{3+} is partially substituted by Al^{3+} suggests that the driving force and ΔG formation energy for Li-ordering is rather modest and easily perturbed by minor doping entropy increase. It was also the case for overlithiated $LiCoO_2$, where even a very little excess of Li found in the Co layers hinders the Li-vacancy ordering at x = 0.5.[33] The absence of this phase transition further confirms that Al is successfully homogeneously introduced into the $LiCoO_2$ lattice.

If charged up to 4.5V vs Li^+/Li, the capacity difference between the two materials is negligible vs. typical coincell method accuracy and precision (198 mAh/g for st-$LiCoO_2$ versus 196 mAh/g for $LiCo_{0.96}Al_{0.04}O_2$), but when charged up to 5V, the Al-doped phase shows a much lower capacity (247 mAh/g) than the undoped one (258 mAh/g) since less Li is deintercalated at 5V from the latter (**Figure 1**).

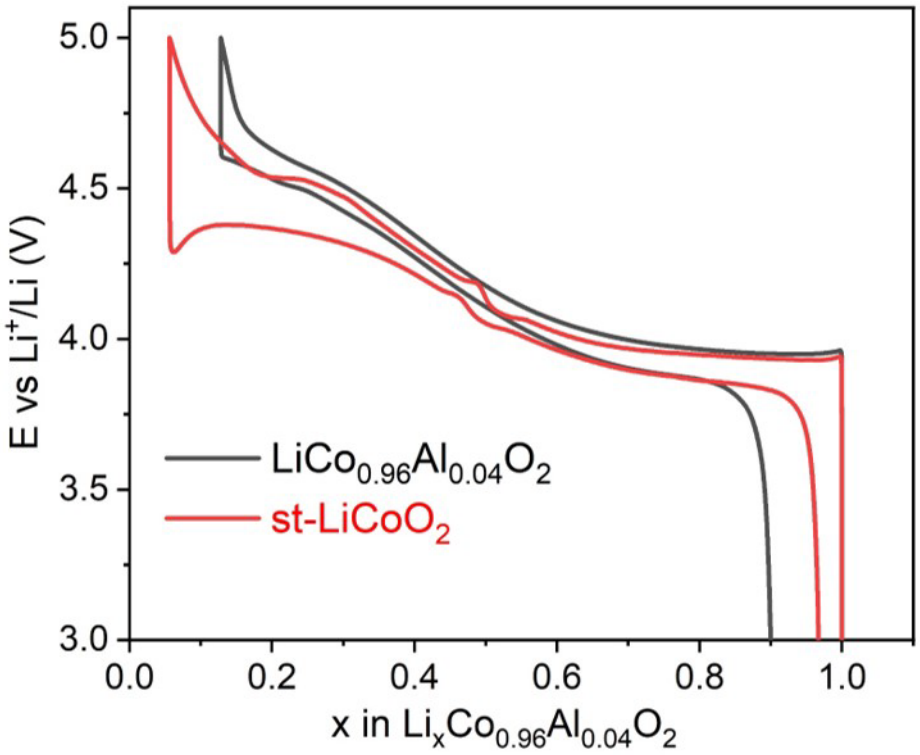

Figure 1: First charge–discharge curves in the 3–5 V voltage range vs. Li^+/Li of $LiCo_{0.96}Al_{0.04}O_2$ and st-$LiCoO_2$ (C/20 cycling rate).

Extended electrochemical tests were further performed in the 3-4.6V range. **Figure 2a** shows the discharge capacity profiles at 1C and C/10 cycling rate followed the testing program provided in Table S1, and **Figure 2b** shows the corresponding discharge capacity evolution for st-$LiCoO_2$ and $LiCo_{0.96}Al_{0.04}O_2$. It appears that Al doping limits the capacity fading. Indeed, as Al-doping acts as top of charge limiter,[29] when cycling up to 4.6V at C/10, the Li concentration reached in the two materials significantly differs: $Li_{0.15}CoO_2$ and $Li_{0.22}Co_{0.96}Al_{0.04}O_2$. Thus, the 8th discharge displayed on **Figure 2** performed at 1C leads to very different 220 and 180 $mAhg^{-1}$ capacities for st-$LiCoO_2$ and $LiCo_{0.96}Al_{0.04}O_2$ respectively. The capacity retention is better for the Al-doped compound, as the time spent at high state of charge and the unit cell volume contraction is less for $LiCo_{0.96}Al_{0.04}O_2$ compared to st-$LiCoO_2$. A strict comparison of cycle life for a same state of charge would require $LiCo_{0.96}Al_{0.04}O_2$ to be cycled at a higher voltage.

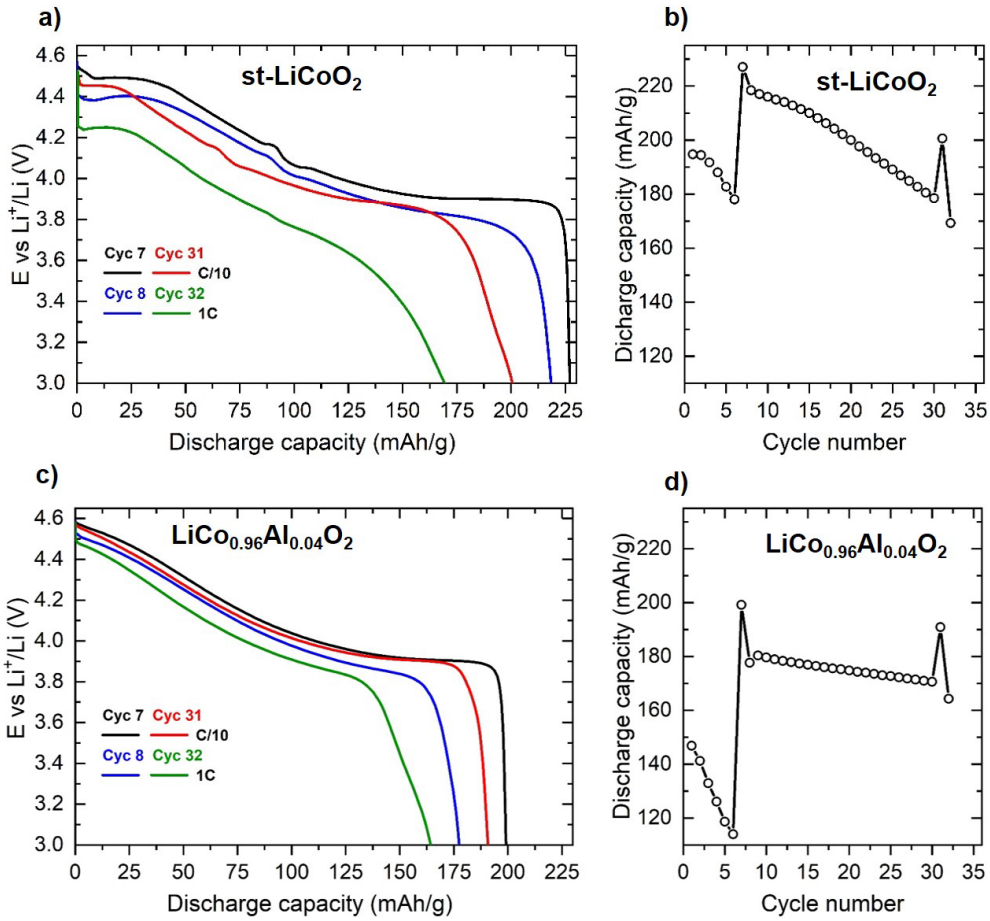

Figure 2 : Discharge profiles (3V-4.6V) of Li//$LiMO_2$ (M=Co, Al) cells observed for the 7, 8, 31 and 32th cycles of a) st-$LiCoO_2$ and c) $LiCo_{0.96}Al_{0.04}O_2$ using cycling conditions provided in **Table S1**. Corresponding discharge capacities versus cycle number of b) st-$LiCoO_2$ and d) $LiCo_{0.96}Al_{0.04}O_2$.

In order to have a general overview of the mechanisms involved during charging, XRD and NMR study were performed on deintercalated samples prepared using a galvanostatic charge (C/20 rate) applied up to the desired Li content (x) followed by a relaxation step (**Figure S5**). The XRD patterns of the $Li_xCo_{0.96}Al_{0.04}O_2$ and Li_xCoO_2 materials are shown in **Figure S6 and S7**. Special attention was given to the (003) diffraction peak evolution that allows to directly follow the changes in the interslab distance, related to the lithium amount and stacking modifications. In the two systems, upon deintercalation this peak shifts towards lower angles upon deintercalation up to x=0.5, and then shifts back to higher angles for lower Li amount. This denotes an expansion of the

structure along the $c_{hex.}$ followed by a contraction (**Table S2**) which is consistent with the literature[4] and commonly observed during the Li de-intercalation of layered Li_xMO_2 materials.[8] The ^{7}Li, ^{27}Al and ^{59}Co MAS NMR spectra evolution versus the Li content are shown in **Figure 3** and **Figure S8**. While Li is in diamagnetic environments for the two pristine $LiCo_{0.96}Al_{0.04}O_2$ and st-$LiCoO_2$ samples, giving rise to signals close to 0 ppm, hyperfine interactions due to the oxidation of LS-Co^{3+} ($t_{2g}^6e_g^0$) to LS-Co^{4+} ($t_{2g}^5e_g^0$) ions are expected for the deintercalated samples.

The results observed for Li_xCoO_2 samples are in good agreement with the literature.[9,39] As x decreases at the early stage of the charge for $0.95 < x < 1$ (**Figure S8**), the intensity of the 0 ppm signal decreases, due to a strong hyperfine interaction between the single electron of the formed LS-Co^{4+} ($t_{2g}^5e_g^0$) ions and adjacent Li nuclei. Ménétrier et al.[9] interpreted this intensity decrease by the localized character of the single electron of Co^{4+}, found in one of the t_{2g} orbitals pointing directly towards adjacent lithium 2s orbital through the common edge of the CoO_6 and LiO_6 octahedra. Upon further lithium removal (**Figure 3**), a very weak new signal appears at 61 ppm for $x = 0.95$ and increases in intensity at the expense of the 0 ppm signal. This signal then shifts to higher ppm values until x=0.5. Ménétrier et al.[9] attributed this new signal to a Knight interaction due to the participation of the 2s orbital of lithium at the Fermi level, in good agreement with the metallic character of Li_xCoO_2 phases for $x < 0.74$.[9] NMR is thus sensitive to the change in nature of the hyperfine interaction from localized electronic spins (Fermi contact) to delocalized ones (Knight shift). For $x < 0.5$, the Knight shifted signal is displaced back towards lower ppm values as also observed by Shimoda et al. [40] The global evolution of the Li signal position versus x results from an interplay between the change in the local electronic structure (number of formal Co^{4+} ions and localized versus delocalized electron spin character) and the change of local geometric structure (overall Li-O-Co distances or angles evolution).

Figure S8 shows that the observation of the ^{27}Al and ^{59}Co MAS NMR signals is rapidly loss while deintercalating Li^+ ions : the signals vanish for $x = 0.80$ and $x = 0.95$, respectively for ^{27}Al and ^{59}Co NMR. These signal loss could come from a strong Fermi contact interaction (localized state) and a stronger contribution of the s orbitals of Al and Co at the Fermi level compared to Li (delocalized state). For those nuclei, either a very broad signal not detected in our conditions or a very fast relaxation beyond the NMR timescale are to be expected. Therefore, no information from ^{27}Al and ^{59}Co MAS NMR regarding the local structure in samples prepared at high voltage could be obtained.

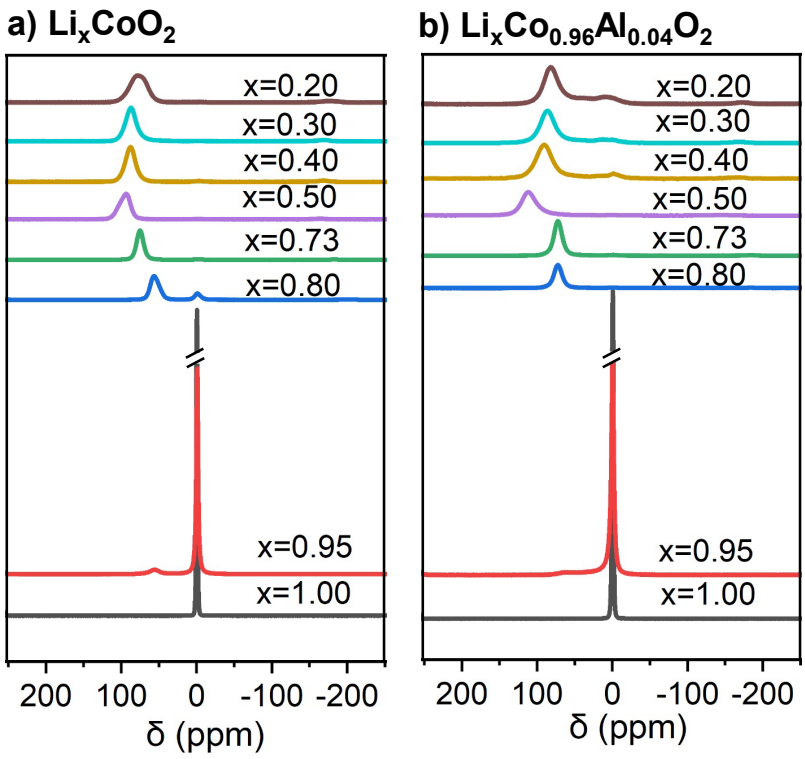

Figure 3: Ex-situ ^{7}Li MAS NMR spectra for a) Li_xCoO_2 and b) $Li_xCo_{0.96}Al_{0.04}O_2$ recorded using a rotor-synchronized Hahn echo sequence (ν_R = 30 kHz). Arbitrary intensities are used here to better visualize the shifts.

3.3 Detailed study in the high voltage region

In order to discuss the effect of the state of charge (Li content) and of the cutoff voltage, samples have been prepared following two routes as described in the experimental section: using a galvanostatic charge applied up to the desired Li content (x) followed by a relaxation step (**Figure S5**) and using a galvanostatic charge applied up to the desired voltage followed by a floating step until the current reached ~ 0 mA (**Figure S9**). The first route allows comparing samples prepared at the same state of charge, but prepared at different voltages that might induce different electrolyte degradation and the second route allows comparing phases at equilibrium for a given voltage but with different Li content. In addition, this second route leads to more aged samples since they spend more time at high voltage during the floating step.

3.3.1 $Li_xCo_{0.96}Al_{0.04}O_2$ and Li_xCoO_2 samples prepared at the same states of charge

The XRD patterns of $Li_xCo_{0.96}Al_{0.04}O_2$ and Li_xCoO_2 are provided in **Figure S6**. In the $Li_xCo_{0.96}Al_{0.04}O_2$, system, the x=0.5 and x=0.4 samples can be indexed using a single O3 type phase. However, for x=0.3, the co-existence of two (00l) lines indicates the presence of two phases that can be both indexed using the R-3m space, suggesting the presence of O3 and H1-3 phases. Those two phases are still present for x = 0.2, but, for this composition, the XRD pattern shows much broader line, which could be explained by the existence of stacking faults within the layered oxide.[41] In the case of st-$LiCoO_2$, a pure O3 phase is observed for $0.5 < x \leq 0.3$ and three phases coexist for x=0.2 namely O3, H1-3 and another phase with an intermediate interslab space that can results from an intergrowth of O3 and H1-3 stackings. Note that such in intermediate phase was not observed during operando measurements and might be formed only during the relaxation step.[42] In the two systems, no signature of the formation of the O1 phase (P3m1 space group with a_{hex} = 2.822 Å and c_{hex} = 4.29 Å) phase has been observed for compounds prepared up to x = 0.2.

Figure 4a and **4b** shows the ^{7}Li NMR spectra of the deintercalated samples from st-$LiCoO_2$ and from $LiCo_{0.96}Al_{0.04}O_2$. The spectra of the $Li_{0.5}CoO_2$ and $Li_{0.5}Co_{0.96}Al_{0.04}O_2$ phases are rather similar with a Knight shifted signal located at 94 ppm and 112 ppm respectively. For lower Li content, however, the spectra differ significantly.

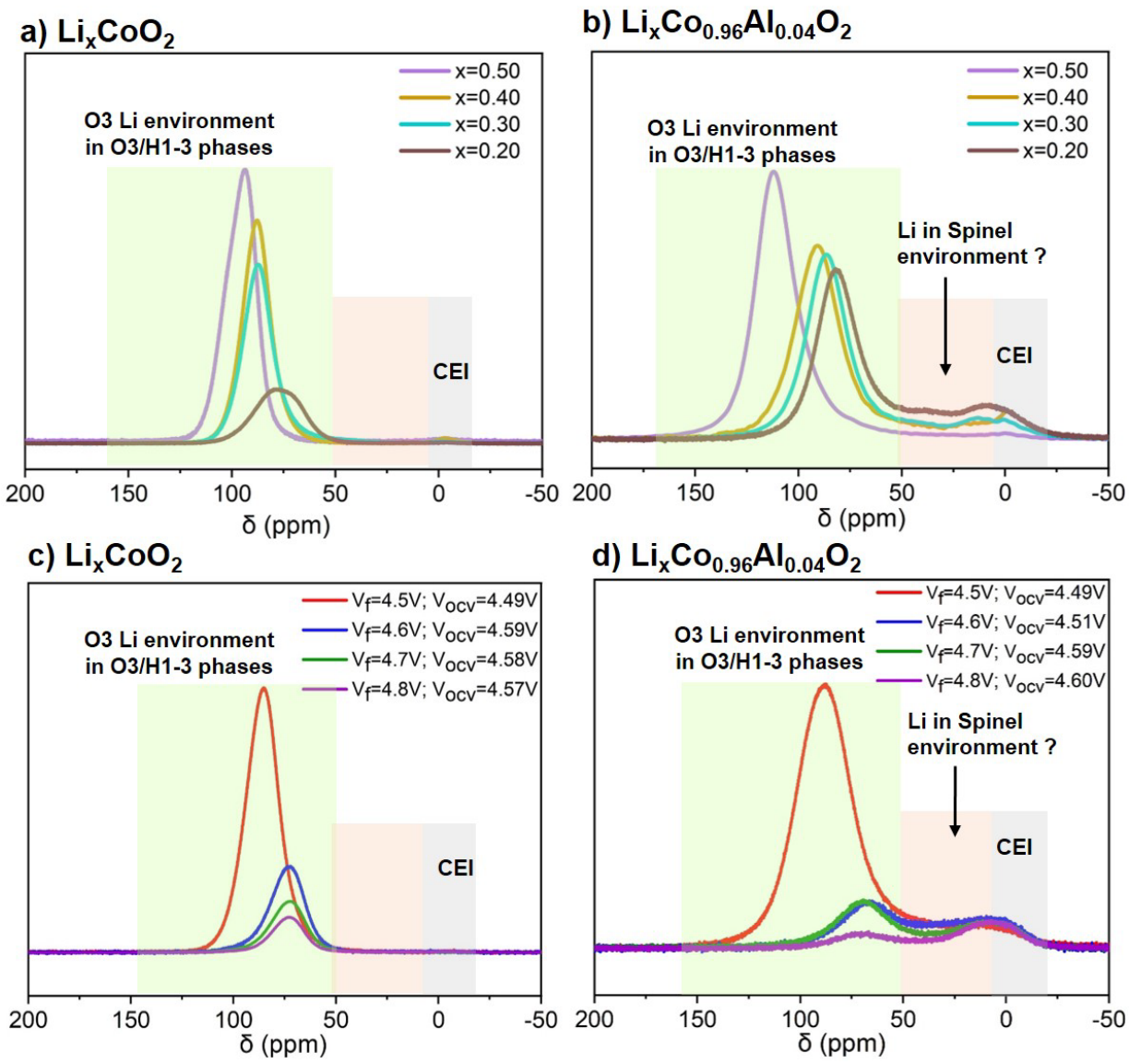

Figure 4: Comparison of ^{7}Li MAS NMR for highly deintercalated phases of a) Li_xCoO_2 and b) $Li_xCo_{0.96}Al_{0.04}O_2$ with fixed Li contents of c) Li_xCoO_2 and d) $Li_xCo_{0.96}Al_{0.04}O_2$ with fixed floating voltages. The ex situ NMR spectra intensities were normalized with respect to the mass of the sample analyzed and number of scans.

In the Li_xCoO_2 system, the signal shifts to lower ppm values with a strong decrease in intensity and a broadening of the signal for x=0.2 as seen on **Figure 4a**.[39] This signal is assigned to Li in the O3-type environment, expected to be similar in the H1-3 stacking locally if we assume that a negligible amount of Li is present in the O1 interslab space. The broad signal for x = 0.2 may be due to the co-existence of 3 phases for this materials as seen by XRD, that probably exhibit

slightly different compositions leading to different shifted signals. No rapid exchange is therefore observed at the NMR timescale between those domains.

In the $Li_xCo_{0.96}Al_{0.04}O_2$ system, the main signal assigned to Li in O3 and H1-3 phases also shifts to lower ppm values, and for $x < 0.3$, new contributions appear in the [-20;50] ppm range with significant intensity (**Figure 4b**). Signals located in 10-50 ppm could be attributed to Li in spinel-type environment as a first approximation according to Godillot et al. [43], this point will be discussed in detail below. Additionally, signals located around 0 ppm can be assigned to diamagnetic lithium environments from the CEI (Cathode Electrolyte Interphases). Note that the signal intensity of the $Li_{0.2}Co_{0.96}Al_{0.04}O_2$ is larger than expected from the composition, indicating the participation of the electrolyte decomposition parasitic reaction in agreement with the presence of significant signals of Li in the CEI.

3.3.2 $Li_xCo_{0.96}Al_{0.04}O_2$ and Li_xCoO_2 samples prepared at the same voltages

The Li content of the materials prepared with different cutoff voltages (4.5V, 4.6V, 4.7V and 4.8V) is difficult to estimate due to the parasitic reaction of the electrolyte degradation, but are respectively lower than 0.32, 0.17, 0.10, 0.09 for Li_xCoO_2 (**Figure S9a**) and 0.32, 0.24, 0.18, 0.15 for $Li_xCo_{0.96}Al_{0.04}O_2$ (**Figure S9b**). The last two compositions exhibit therefore lower Li contents than samples of the previous section. One can observe that for floating voltages $V_f \geq 4.6$ V, the cell voltage dropped significantly (V_{OCV} as opposed to V_f) when the cell was disconnected. Indeed, the highest reached V_{ocv} is only 4.6V, which remains higher than the voltage observed for the materials prepared without floating (**Figure S.1**). A really similar behavior was observed for the Li_xCoO_2 samples prepared in the same way, but the 4.6V voltage remains stable after disconnecting the cell ($V_{OCV} \approx V_f$), whereas the voltage drops to 4.51V for the Al doped compound. The different materials were then characterized by XRD (**Figure S10**) and ^{7}Li MAS NMR (**Figure 4c and 4d**). All diffraction peaks for materials prepared at V_f=4.5 V can be indexed based on the O3 structure with rather similar Li content ($Li_{0.24}Co_{0.96}Al_{0.04}O_2$ and $Li_{0.27}CoO_2$ if one neglects the electrolyte degradation at this voltage). For the materials prepared at V_f=4.6V, two peaks are observed for Li_xCoO_2 at 2θ=19.76° and 2θ=20.34°, which correspond respectively to the $(006)_{H1\text{-}3}$ and $(00\ell)_{int}$ diffraction lines of the H1-3 and intermediate phase between H1-3 and O1 type structures as detected also by operando XRD.[42] Only the $(006)_{H1\text{-}3}$ diffraction line is observed in the case of the Al-doped sample at the same V_f=4.6V. At 4.7V, three very broad contributions are observed for

Li_xCoO_2 assigned to the $(006)_{H1-3}$, $(00\ell)_{int}$ and $(001)_{O1}$ diffraction lines, indicating structures with a high density of stacking faults, resulting in overall structural disorder. In the case of the Al doped compounds, the $(006)_{H1-3}$ peak remains narrow and the $(001)_{O1}$ diffraction line appears at $2\theta=20.92°$ for $V_f \geq 4.7V$. Finally, Li_xCoO_2 prepared at 4.8V also exhibits broad diffraction line assigned to a defected H1-3 phase with $x \leq 0.09$ and $Li_xCo_{0.96}Al_{0.04}O_2$ exhibits broad diffraction lines assigned to H1-3 and O1 phases with an overall Li content $x \leq 0.15$.

From ^{7}Li MAS NMR (**Figure 4c and 4d**), spectra of the materials prepared at V_f=4.5V are very similar to the ones of, respectively, $Li_{0.3}CoO_2$ and $Li_{0.3}(Co_{0.96}Al_{0.04})O_2$ phases, with a single Knight shifted signal located around ~75 ppm. For the three samples prepared at larger floating voltages $V_f \geq 4.6V$, the line shape of the ^{7}Li signal of Li_xCoO_2 samples remains almost unchanged (**Figure 4c**). Several contributions are observed for $Li_xCo_{0.96}Al_{0.04}O_2$ samples (**Figure 4d**) as already discussed above, but in different relative amounts. The intensity of the signal located in the [~50-130] ppm range expected for Li in the O3 and H1-3 phases strongly decreases while the intensity of signals corresponding to Li in (supposedly) spinel type environment at [10-50] ppm and to Li in the CEI around 0 ppm remain essentially the same.

The ^{7}Li MAS NMR results suggest that the CEI formed at high voltage could be either very thin or unstable for st-$LiCoO_2$, and may be dissolved by the electrolyte solvent after the cell disconnection or by the electrode washing step using DMC prior to our measurements. Additionally, no signal associated to a lithiated spinel phase was detected in this case. As opposed to st-$LiCoO_2$, new local Li environments potentially assigned to both a disordered (as not seen by XRD) spinel-like lithiated phase and a stable CEI were observed for $Li_xCo_{0.96}Al_{0.04}O_2$. These features could explain the higher stability upon cycling of the Al-doped samples and their highest irreversible capacity during the first cycle.

3.3.3 Structural characterization after cycling at high voltage (3 cycles)

To further understand the performance of $LiCo_{0.96}Al_{0.04}O_2$ at high voltage, this material was charged-discharged 3 times between 3V and 4.8V with a C/20 rate then recovered at the end of discharge after a floating at 3V (**Figure S11a**). The sample was then characterized by XRD, MAS NMR and TEM. XRD and NMR data of this new sample was compared to the data collected for

the pristine phase and a $Li_{0.98}Co_{0.96}Al_{0.04}O_2$ prepared by galvanostatic charge, as the phase at this composition is found to have cell parameters very close to the ones of the material recovered after 3 cycles (**Figure S11b and Table S3**). The XRD patterns of the 3 compounds, that can be indexed using a single phase in the R-3m space group of the O3 stacking. From the electrochemical curve (**Figure S11a)**, a x=0.95 value was predicted, but, the cell undergoes some electrolyte decomposition at high voltage that shifted slightly the cycling curves on the left.

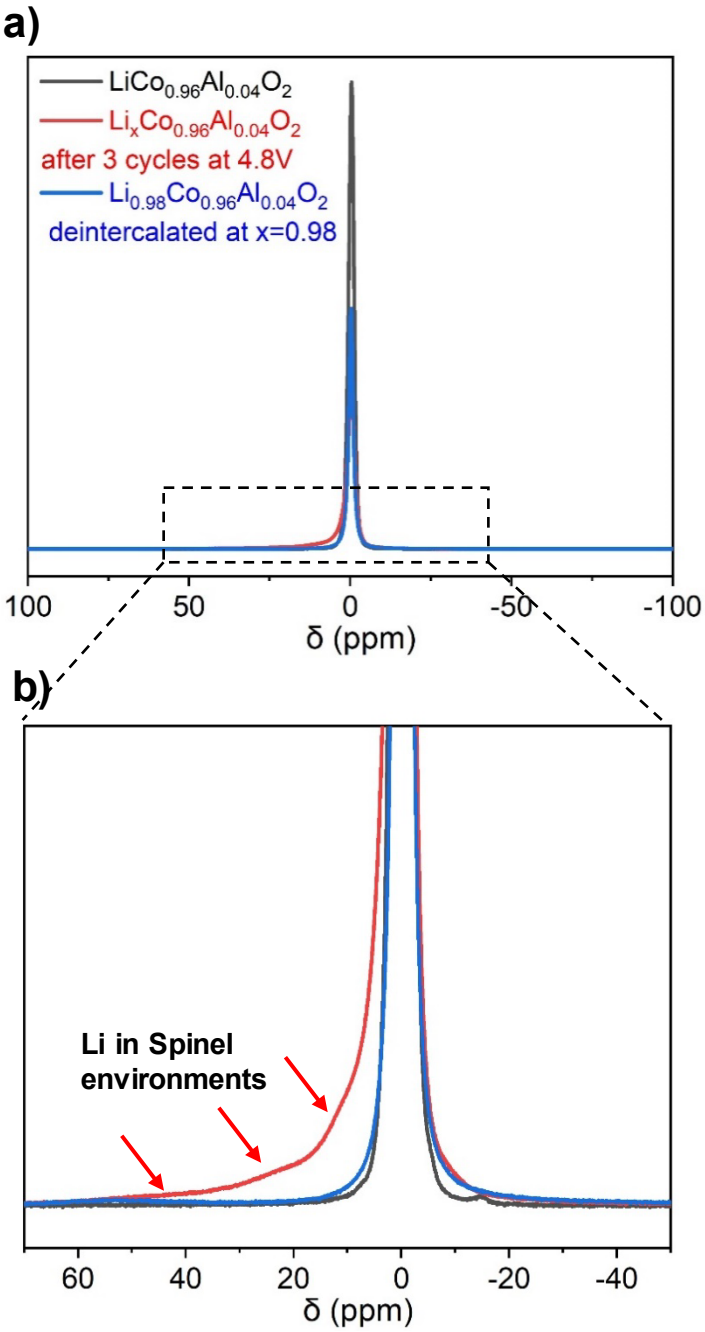

Figure 5: a) Ex-situ ^{7}Li solid-sate MAS NMR of the $Li_xCo_{0.96}Al_{0.04}O_2$ and b) zoom of the spectra.

In **Figure 5a**, a strong signal located near 0 ppm assigned to Li in the O3 phase surrounded by diamagnetic LS-Co^{3+} ions is clearly observed for the $Li_xCo_{0.96}Al_{0.04}O_2$ sample recovered after 3 cycles up to 4.8V, similarly to the x = 1 and x = 0.98 samples. Additional new signals located at 12 ppm, 25 ppm and 43 ppm can also be observed. Signals in this range have already been observed

for highly deintercalated materials and were attributed to Li in spinel-like environment as a first approximation. According to Godillot et al.[43] the 12 ppm and 24 ppm signals are assigned to Li in the 8a tetrahedral sites of the spinel structure, that may differ from their Co/Al local environments here and the 43 ppm signal is assigned to Li in the 16c octahedral sites. No secondary phase was detected by XRD indicating that the spinel-type phase is either very disordered phase or only present at a very local scale (**Figure S11b**). ^{59}Co and ^{27}Al MAS NMR is not really informative regarding the spinel formation since a loss of signals for those phases is expected : in Co_3O_4, an electronic delocalization occurs on Co ions leading to a very strong hyperfine interaction with ^{59}Co nuclei that directly carries the electronic spins; in $CoAl_2O_4$, the hyperfine interaction between the Co^{2+} ions and the ^{27}Al nuclei is also very strong and the absence of signal for Al was already reported[44] and was also confirmed by our group while heat treating Co_3O_4 with Al_2O_3 at 1000 °C.[37] Indeed, the ^{59}Co and ^{27}Al MAS NMR spectra of the $Li_xCo_{0.96}Al_{0.04}O_2$ sample recovered after 3 cycles up to 4.8V are really similar to the ones of the x= 0.98 sample, so no major structural modification occurs within the O3 phase (**Figure 6**).

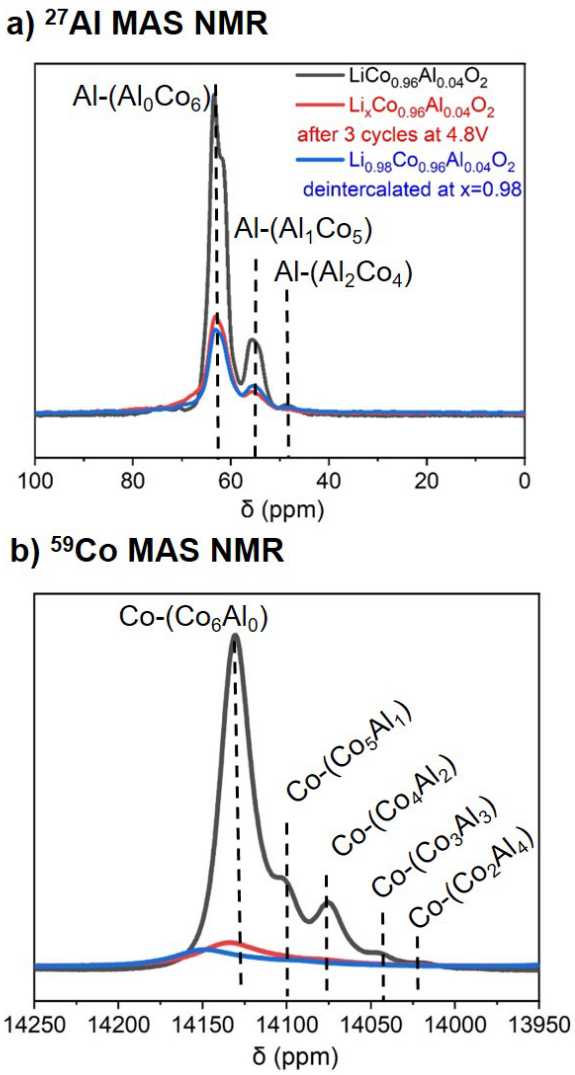

Figure 6: a) ^{27}Al and b) ^{59}Co MAS NMR of $Li_xCo_{0.96}Al_{0.04}O_2$ cycled 3 times between (3V-4.8V) and recovered after a floating at 3V compared to the pristine and the deintercalated $Li_{0.98}Co_{0.96}Al_{0.04}O_2$.

TEM was used to confirm the hypothesis of the existence of a spinel phase in the cycled $Li_xCo_{0.96}Al_{0.04}O_2$ material and to spatially localize it. **Figure 7a**, shows a nano-beam electron diffraction pattern obtained from the center of one crystal of the cycled $Li_xCo_{0.96}Al_{0.04}O_2$ material (**Figure 7c**). This diffraction pattern corresponds to the [211] zone axis of the $LiCo_{0.96}Al_{0.04}O_2$ phase using the hexagonal axis system (R-3m space group). When the nano-beam is displaced from the center to the edge of the crystal (**Figure 7f**), another pattern is obtained (**Figure 7d**). The

presence of a spinel type phase has to be considered to explain it. Indeed, all the reflections of this pattern can be indexed by considering the [112] spinel zone axis as demonstrated by the superposition of the experimental pattern with the [112] spinel zone axis simulated pattern (**Figure 7e**). Nevertheless, note that some reflections have much higher intensities than others. These intense reflections seem to match those observed in the center of the crystal and indeed, some interplanar distances are identical in both structures as for instance $d_{1\text{-}20lay}$ and $d_{4\text{-}40spi}$ or $d_{\text{-}204lay}$ and $d_{\text{-}1\text{-}11spi}$. The pattern obtained on the edge of the crystal must then be considered as the superposition of patterns belonging to both lamellar and spinel structures. This finding is thus in line with our ^{7}Li MAS NMR study indicating the presence of spinel-like environments for Li and additionally reveals that those domains are present at the surface of the particles only.

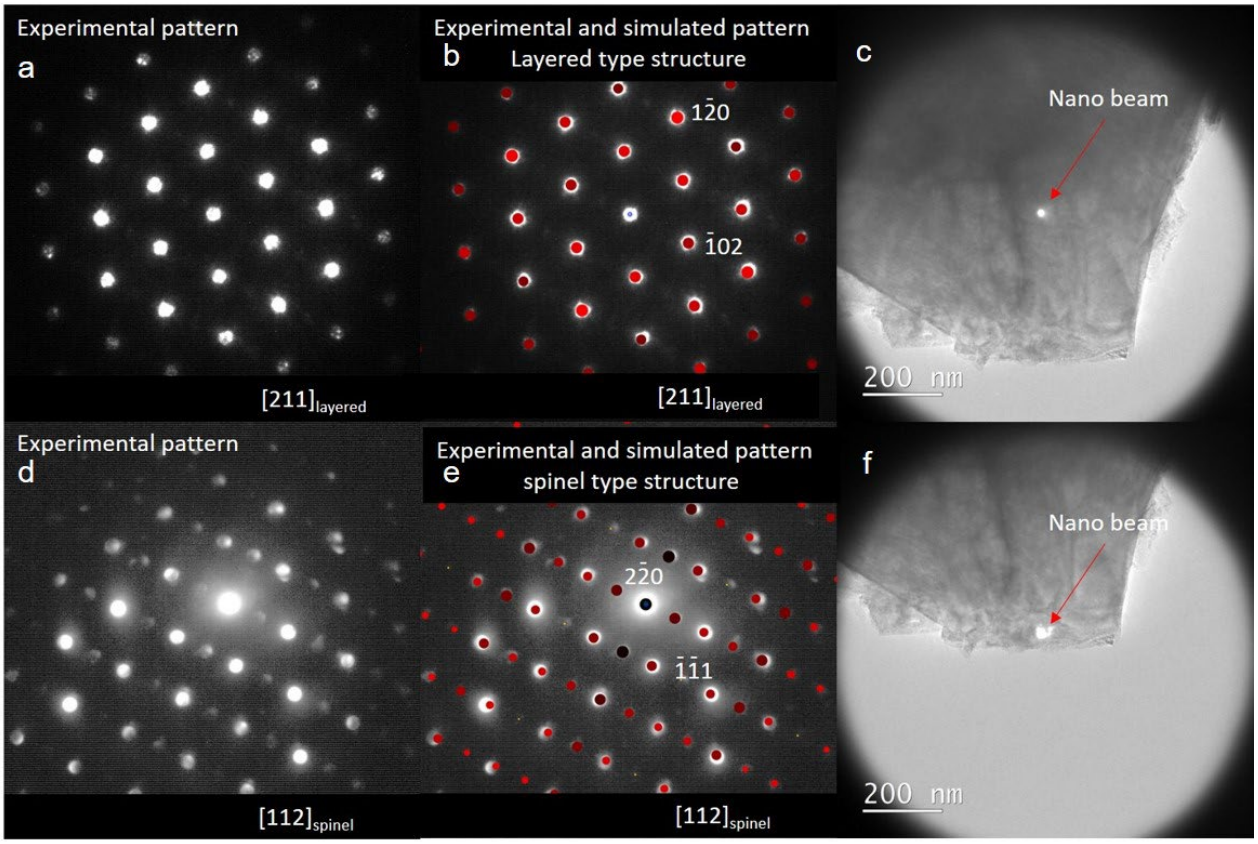

Figure 7: Nanobeam electron diffraction on the cycled $Li_xCo_{0.96}Al_{0.04}O_2$. a) Experimental diffraction pattern related to the center of the particle indexed with the $Li_xCo_{0.96}Al_{0.04}O_2$ structure. b) Comparison of experimental and simulated patterns. c) Location of the beam corresponding to pattern a. d) Experimental diffraction pattern related to the edge of the particle

indexed with a spinel type structure. e) Comparison of experimental and simulated pattern and f) location of the beam corresponding to pattern d.

4 Discussion and conclusions

$LiCo_{0.96}Al_{0.04}O_2$ was synthesized by a specific solid state route. ^{27}Al MAS NMR and XRD studies revealed that the Al-doping in this material is homogeneous while ^{7}Li MAS NMR indicates that its stoichiometry (Li/M=1.00) is ideal. Our electrochemical cycling study in Li cells reveals that even a low substituted amount of Co with Al (4%) has a profound effect on the electrochemical performance and yields a better cycling stability in the 3-4.6 V voltage range. XRD and ^{7}Li MAS NMR studies revealed that up to 4.5 V vs Li^+/Li, the overall structural evolution of the $LiCo_{0.96}Al_{0.04}O_2$ and st-$LiCoO_2$ phases is similar, although i) the insulator-metal transition does not occur in the same composition range and ii) the monoclinic distortion at x = 0.5 is hindered by Al doping. At higher voltages (> 4.6 V vs. Li^+/Li), noticeable structural differences have been evidenced in the deintercalated $Li_xCo_{0.96}Al_{0.04}O_2$ and Li_xCoO_2 materials and may be responsible for the enhanced cycling stability of Al-doped $LiCoO_2$. The XRD study shows that the deintercalated phases prepared for $x < 0.2$ from st-$LiCoO_2$, either by fixing the Li content or by a floating method, present the co-existence of several phases (O3, H1-3, O1 and phases with intermediate interslab space) with stacking faults. Whereas, deintercalated samples prepared from $LiCo_{0.96}Al_{0.04}O_2$ are more crystalline, and the formation of phases with intermediate interslab space is not observed. In addition, at 4.6V, the O1 phase is not observed for the Al-doped sample.

More interestingly, ^{7}Li MAS NMR reveals very different Li local environments in the high voltage phases. Unlike Li_xCoO_2, for Al-doped phases, signals assigned to Li in spinel-like environments and in a diamagnetic CEI layer are observed in addition to the signal corresponding to Li in the interslab space of the O3 /H1-3 structures. Those observations do not depend on the materials preparation (by fixing the Li content or the floating voltage). The spinel phase is still detected after a few cycles in discharged $LiCo_{0.96}Al_{0.04}O_2$ phase is and the TEM study revealed that it is located at the surface of the particles. Since only signals of Li in the interslab space of the O3 or H1-3 structure were observed for Li_xCoO_2, we believe that the CEI formed on that material has a different nature and is unstable (either dissolved after the cell disconnection or by the electrode

washing step prior to the measurements).[45] The different reactivity of the surface of $LiCoO_2$ and Al-doped $LiCoO_2$ has already been reported in literature: the basic character of the $LiCo_{1-x}Al_xO_2$ surface makes these materials less reactive than $LiCoO_2$ toward acidic species (such as HF) that are present in $LiPF_6$-based electrolytes.[46] The strong polarization observed at the beginning of the discharge from 5V in the st-$LiCoO_2$ system might therefore result from i) the high resistivity character of that CEI at high voltage that may dissolve then while discharging as unstable; ii) the formation of the H1-3 or O1 phase at the particles surface with a low interslab space that may also prevent a good Li^+ ions diffusivity back to the particles.

Based on our study, we believe that Al-doping improves the cycling performance of $LiCoO_2$ up to 4.6V, mainly by modifying the particles surface evolution upon cycling at high voltages. Even during the first charge, it leads to the formation of a surface reconstruction with the formation of a lithiated spinel-type phase that should have a good ionic conductivity. In the case if $LiCoO_2$, the formation of a spinel phase has been also reported,[47] is either not lithiated as not detected by ^{7}Li MAS NMR or formed only upon extended cycling. The lithiated spinel phase formed on the Al-doped compound, may then react differently with the electrolyte to form a stable CEI layer, whose composition is different from the one formed on Li_xCoO_2. The formation of the Li-containing spinel phase and a stable CEI at the surface of the particles probably also explains the strong reduction of Co dissolution observed at high voltage as reported by Myung et al.[31]

ASSOCIATED CONTENT

Supporting Information

XRD patterns and ^{7}Li, ^{27}Al and ^{59}Co MAS NMR of the two pristine samples together with a comparison with statistical expected intensities for ^{27}Al NMR; First Cycling curve of st-$LiCoO_2$ indicating the different phases; Cycling conditions used for Figure 2; Galvanostatic charge curves for the preparation of the deintercalated Li_xCoO_2 and $Li_xCo_{0.96}Al_{0.04}O_2$ phases; XRD patterns and cell parameters of the deintercalated Li_xCoO_2 and $Li_xCo_{0.96}Al_{0.04}O_2$ phases; ^{7}Li, ^{27}Al and ^{59}Co MAS NMRS spectra of the $Li_xCo_{0.96}Al_{0.04}O_2$ phases for $0.73 \leq x \leq 1$; Galvanostatic charge curves followed by a floating step at different voltages for the preparation of the deintercalated Li_xCoO_2 and $Li_xCo_{0.96}Al_{0.04}O_2$ phases; XRD patterns of the phases prepared at a given voltage $V \geq 4.5V$;

Three first cycles (3V-4.8V) of $LiCo_{0.96}Al_{0.04}O_2$ and XRD pattern of the $Li_xCo_{0.96}Al_{0.04}O_2$ phase recovered at the end of discharge compared to the pristine and the deintercalated $Li_{0.98}Co_{0.96}Al_{0.04}O_2$.

AUTHOR INFORMATION

Corresponding Author

Dany Carlier – Univ. Bordeaux, CNRS, Bordeaux INP, ICMCB, UMR 5026, F-33600 Pessac, France; orcid.org/0000-0002-5086-4363

Authors

Fatima-Ezzahra Er-Rami – Univ. Bordeaux, CNRS, Bordeaux INP, ICMCB, UMR 5026, F-33600 Pessac, France; Umicore Rechargeable battery materials, 31 rue du marais, Brussels BE-1000, Belgium ; https://orcid.org/0000-0002-0616-2161

Marie Duffiet – Univ. Bordeaux, CNRS, Bordeaux INP, ICMCB, UMR 5026, F-33600 Pessac, France; Umicore Rechargeable battery materials, 31 rue du marais, Brussels BE-1000, Belgium

Sean Hinkle – Univ. Bordeaux, CNRS, Bordeaux INP, ICMCB, UMR 5026, F-33600 Pessac

Jérémie Auvergniot – Umicore Rechargeable battery materials, 31 rue du marais, Brussels BE-1000, Belgium

Maxime Blangero – Umicore, Materials Research and Development, Cheonan-Shi, Chungnam-Do 330-200, Korea

Pierre-Etienne Cabelguen –Umicore Rechargeable battery materials, 31 rue du marais, Brussels BE-1000, Belgium ; https://orcid.org/0000-0002-5953-4213

KyeongSe Song – Umicore, Materials Research and Development, Cheonan-Shi, Chungnam-Do 330-200, Korea

François Weill – Univ. Bordeaux, CNRS, Bordeaux INP, ICMCB, UMR 5026, F-33600 Pessac ; https://orcid.org/0000-0001-8331-6075

Claude Delmas – Univ. Bordeaux, CNRS, Bordeaux INP, ICMCB, UMR 5026, F-33600 Pessac ; https://orcid.org/0000-0002-8188-0067

ACKNOLEDGEMENTS

The authors wish to thank Umicore company for financial support and fruitful discussions and Cathy Denage for experimental support and SEM image acquisition.

References

(1) Mizushima, K.; Jones, P. C.; Wiseman, P. J.; Goodenough, J. B. Li_xCoO_2 (0. *Mater. Res. Bull.* **1980**, *15* (6), 783–789. https://doi.org/10.1016/0025-5408(80)90012-4.

(2) Wang, L.; Chen, B.; Ma, J.; Cui, G.; Chen, L. Reviving Lithium Cobalt Oxide-Based Lithium Secondary Batteries-toward a Higher Energy Density. *Chem. Soc. Rev.* **2018**, *47* (17), 6505–6602. https://doi.org/10.1039/C8CS00322J.

(3) Orman, H. J.; Wiseman, P. J. Cobalt(III) Lithium Oxide, $CoLiO_2$: Structure Refinement by Powder Neutron Diffraction. *Acta Crystallogr. Sect. C* **1984**, *40* (1), 12–14. https://doi.org/https://doi.org/10.1107/S0108270184002833.

(4) Reimers, J. N.; Dahn, J. R. Electrochemical and in Situ X-Ray Diffraction Studies of Lithium Intercalation in Li_xCoO_2. *J. Electrochem. Soc.* **1992**, *139* (8), 2091–2097.

(5) Ohzuku, T.; Ueda, A. Solid-State Redox Reactions of $LiCoO_2$ (R3m) for 4 Volt Secondary Lithium Cells. *J. Electrochem. Soc.* **1994**, *141* (11), 2972–2977.

(6) Delmas, C.; Fouassier, C.; Hagenmuller, P. Structural Classification and Properties of the Layered Oxides. *Phys. BC* **1980**, *99* (1), 81–85. https://doi.org/10.1016/0378-4363(80)90214-4.

(7) Ven, A. V. der; Aydinol, M. K.; Ceder, G. First-Principles Evidence for Stage Ordering in Li_xCoO_2. *J. Electrochem. Soc.* **1998**, *145* (6), 2149. https://doi.org/10.1149/1.1838610.

(8) Van der Ven, A.; Aydinol, M. K.; Ceder, G.; Kresse, G.; Hafner, J. First-Principles Investigation of Phase Stability in Li_xCoO_2. *Phys. Rev. B* **1998**, *58* (6), 2975–2987. https://doi.org/10.1103/PhysRevB.58.2975.

(9) Ménétrier, M.; Saadoune, I.; Levasseur, S.; Delmas, C. The Insulator-Metal Transition upon Lithium Deintercalation from $LiCoO_2$: Electronic Properties and ^7Li NMR Study. *J. Mater. Chem.* **1999**, *9* (5), 1135–1140.

(10) Ménétrier, M.; Carlier, D.; Blangero, M.; Delmas, C. On "Really" Stoichiometric $LiCoO_2$. *Electrochem. Solid-State Lett.* **2008**, *11* (11), A179. https://doi.org/10.1149/1.2968953.

(11) Shao-Horn, Y.; Levasseur, S.; Weill, F.; Delmas, C. Probing Lithium and Vacancy Ordering in O3 Layered Li_xCoO_2 ($x \approx 0.5$). *J. Electrochem. Soc.* **2003**, *150* (3), A366. https://doi.org/10.1149/1.1553787.

(12) Yano, A.; Shikano, M.; Ueda, A.; Sakaebe, H.; Ogumi, Z. $LiCoO_2$ Degradation Behavior in the High-Voltage Phase Transition Region and Improved Reversibility with Surface Coating. *J. Electrochem. Soc.* **2017**, *164* (1), A6116–A6122.

(13) Yazami, R.; Ozawa, Y.; Gabrisch, H.; Fultz, B. Mechanism of Electrochemical Performance Decay in $LiCoO_2$ Aged at High Voltage. *Electrochimica Acta* **2004**, *50* (2–3), 385–390. https://doi.org/10.1016/j.electacta.2004.03.048.

(14) Xia, H.; Lu, L.; Meng, Y. S.; Ceder, G. Phase Transitions and High-Voltage Electrochemical Behavior of $LiCoO_2$ Thin Films Grown by Pulsed Laser Deposition. *J. Electrochem. Soc.* **2007**, *154* (4), A337. https://doi.org/10.1149/1.2509021.

(15) Takamatsu, D.; Koyama, Y.; Orikasa, Y.; Mori, S.; Nakatsutsumi, T.; Hirano, T.; Tanida, H.; Arai, H.; Uchimoto, Y.; Ogumi, Z. First In Situ Observation of the $LiCoO_2$ Electrode/Electrolyte Interface by Total-Reflection X-Ray Absorption Spectroscopy. *Angew. Chem. Int. Ed.* **2012**, *51* (46), 11597–11601. https://doi.org/10.1002/anie.201203910.

(16) Pender, J. P.; Jha, G.; Youn, D. H.; Ziegler, J. M.; Andoni, I.; Choi, E. J.; Heller, A.; Dunn, B. S.; Weiss, P. S.; Penner, R. M.; Mullins, C. B. Electrode Degradation in Lithium-Ion Batteries. *ACS Nano* **2020**, *14* (2), 1243–1295. https://doi.org/10.1021/acsnano.9b04365.

(17) Birkl, C. R.; Roberts, M. R.; McTurk, E.; Bruce, P. G.; Howey, D. A. Degradation Diagnostics for Lithium Ion Cells. *J. Power Sources* **2017**, *341*, 373–386. https://doi.org/10.1016/j.jpowsour.2016.12.011.

(18) Amatucci, G. G.; Tarascon, J. M.; Klein, L. C. Cobalt Dissolution in $LiCoO_2$-Based Non-Aqueous Rechargeable Batteries. *Solid State Ion.* **1996**, *83* (1), 167–173. https://doi.org/10.1016/0167-2738(95)00231-6.

(19) Chen, Z.; Dahn, J. R. Methods to Obtain Excellent Capacity Retention in $LiCoO_2$ Cycled to 4.5V. *Electrochimica Acta* **2004**, *49* (7), 1079–1090. https://doi.org/10.1016/j.electacta.2003.10.019.

(20) Jiang, Y.; Yan, P.; Yu, M.; Li, J.; Jiao, H.; Zhou, B.; Sui, M. Atomistic Mechanism of Cracking Degradation at Twin Boundary of LiCoO2. *Nano Energy* **2020**, *78*, 105364. https://doi.org/10.1016/j.nanoen.2020.105364.

(21) Jiang, Y.; Qin, C.; Yan, P.; Sui, M. Origins of Capacity and Voltage Fading of $LiCoO_2$ upon High Voltage Cycling. *J. Mater. Chem. A* **2019**, *7* (36), 20824–20831. https://doi.org/10.1039/C9TA06579B.

(22) Hu, G.; Cao, J.; Peng, Z.; Cao, Y.; Du, K. Enhanced High-Voltage Properties of $LiCoO_2$ Coated with $Li[Li_{0.2}Mn_{0.6}Ni_{0.2}]O_2$. *Electrochimica Acta* **2014**, *149*, 49–55. https://doi.org/10.1016/j.electacta.2014.10.072.

(23) Gu, R.; Cheng, T.; Ma, Z.; Qian, R.; Lyu, Y.; Nie, A.; Guo, B. Enhanced Cycling Stability of High Voltage $LiCoO_2$ by Surface Phosphorylation. *J. Alloys Compd.* **2019**, *803*, 348–353. https://doi.org/10.1016/j.jallcom.2019.06.253.

(24) Cho, J.; Kim, C.-S.; Yoo, S.-I. Improvement of Structural Stability of $LiCoO_2$ Cathode during Electrochemical Cycling by Sol-Gel Coating of SnO2. *Electrochem. Solid-State Lett.* **2000**, *3* (8), 362–365.

(25) Zhang, J.-N.; Li, Q.; Ouyang, C.; Yu, X.; Ge, M.; Huang, X.; Hu, E.; Ma, C.; Li, S.; Xiao, R.; Yang, W.; Chu, Y.; Liu, Y.; Yu, H.; Yang, X.-Q.; Huang, X.; Chen, L.; Li, H. Trace Doping of Multiple Elements Enables Stable Battery Cycling of $LiCoO_2$ at 4.6 V. *Nat. Energy* **2019**, *4* (7), 594–603. https://doi.org/10.1038/s41560-019-0409-z.

(26) Liu, Q.; Su, X.; Lei, D.; Qin, Y.; Wen, J.; Guo, F.; Wu, Y. A.; Rong, Y.; Kou, R.; Xiao, X.; Aguesse, F.; Bareño, J.; Ren, Y.; Lu, W.; Li, Y. Approaching the Capacity Limit of Lithium Cobalt Oxide in Lithium Ion Batteries via Lanthanum and Aluminium Doping. *Nat. Energy* **2018**, *3* (11), 936–943. https://doi.org/10.1038/s41560-018-0180-6.

(27) zhao, ruirui; Zhang, J.; Lee, G.-H.; Zhang, K.; Lau, V. W.; Lee, J.-J.; Moudrakovski, I.; Yang, Y.-L.; Zhou, F.; Park, M.; Hung, I.-M.; Kang, Y. The Origin of Heavy Elemental Doping to Relieve the Lattice Thermal Vibration of Layered Materials for High Energy Density Li Ion Cathodes. *J. Mater. Chem. A* **2020**. https://doi.org/10.1039/D0TA03979A.

(28) Levasseur, S.; Ménétrier, M.; Delmas, C. Combined Effects of Ni and Li Doping on the Phase Transitions in Li_xCoO_2 Electrochemical and ^7Li Nuclear Magnetic Resonance Studies. *J. Electrochem. Soc.* **2002**, *149* (12), A1533–A1540. https://doi.org/10.1149/1.1516219.

(29) Ceder, G.; Chiang, Y.-M.; Sadoway, D. R.; Aydinol, M. K.; Jang, Y.-I.; Huang, B. Identification of Cathode Materials for Lithium Batteries Guided by First-Principles Calculations. *Nature* **1998**, *392* (6677), 694.

(30) Jang, Y.-I.; Huang, B.; Wang, H.; Sadoway, D. R.; Ceder, G.; Chiang, Y.-M.; Liu, H.; Tamura, H. $LiAl_yCo_{1-y}O_2$ (R $\bar{3}$m) Intercalation Cathode for Rechargeable Lithium Batteries. *J. Electrochem. Soc.* **1999**, *146* (3), 862–868.

(31) Myung, S.-T.; Kumagai, N.; Komaba, S.; Chung, H.-T. Effects of Al Doping on the Microstructure of $LiCoO_2$ Cathode Materials. *Solid State Ion.* **2001**, *139* (1), 47–56. https://doi.org/10.1016/S0167-2738(00)00828-6.

(32) Levasseur, S. Evidence for Structural Defects in Non-Stoichiometric HT- $LiCoO_2$: Electrochemical, Electronic Properties and ^{7}Li NMR Studies. *Solid State Ion.* **2000**, *128* (1–4), 11–24. https://doi.org/10.1016/S0167-2738(99)00335-5.

(33) Levasseur, S.; Ménétrier, M.; Shao-Horn, Y.; Gautier, L.; Audemer, A.; Demazeau, G.; Largeteau, A.; Delmas, C. Oxygen Vacancies and Intermediate Spin Trivalent Cobalt Ions in Lithium-Overstoichiometric $LiCoO_2$. *Chem. Mater.* **2003**, *15* (1), 348–354. https://doi.org/10.1021/cm021279g.

(34) Duffiet, M.; Blangero, M.; Cabelguen, P. E.; Song, K. S.; Fauth, F.; Delmas, C.; Carlier, D. Probing Al Distribution in $LiCo_{0.96}Al_{0.04}O_2$ Materials Using ^{7}Li, ^{27}Al, and ^{59}Co MAS NMR Combined with Synchrotron X-Ray Diffraction. *Inorg. Chem.* **2020**, *59* (5), 2890–2899. https://doi.org/10.1021/acs.inorgchem.9b03260.

(35) Han, B.; Paulauskas, T.; Key, B.; Peebles, C.; Park, J. S.; Klie, R. F.; Vaughey, J. T.; Dogan, F. Understanding the Role of Temperature and Cathode Composition on Interface and Bulk: Optimizing Aluminum Oxide Coatings for Li-Ion Cathodes. *ACS Appl. Mater. Interfaces* **2017**, *9* (17), 14769–14778. https://doi.org/10.1021/acsami.7b00595.

(36) Duffiet, M. Investigation of Structural Failure Mechanisms of $LiCoO_2$ at High Voltage and Material Optimization through Aluminum Doping. PhD Thesis, Université de Bordeaux, 2019.

(37) Gaudin, E.; Taulelle, F.; Stoyanova, R.; Zhecheva, E.; Alcántara, R.; Lavela, P.; Tirado, J. L. Cobalt(III) Effect on ^{27} Al NMR Chemical Shifts in $LiAl_xCo_{1-x}O_2$. *J. Phys. Chem. B* **2001**, *105* (34), 8081–8087. https://doi.org/10.1021/jp0105948.

(38) Siegel, R.; Hirschinger, J.; Carlier, D.; Matar, S.; Ménétrier, M.; Delmas, C. ^{59}Co and ^{6,7}Li MAS NMR in Polytypes O2 and O3 of $LiCoO_2$. *J. Phys. Chem. B* **2001**, *105* (19), 4166–4174. https://doi.org/10.1021/jp003832s.

(39) Geng, F.; Shen, M.; Hu, B.; Liu, Y.; Zeng, L.; Hu, B. Monitoring the Evolution of Local Oxygen Environments during LiCoO $_2$ Charging *via Ex Situ* ^{17}O NMR. *Chem. Commun.* **2019**, *55* (52), 7550–7553. https://doi.org/10.1039/C9CC03304A.

(40) Shimoda, K.; Murakami, M.; Takamatsu, D.; Arai, H.; Uchimoto, Y.; Ogumi, Z. In Situ NMR Observation of the Lithium Extraction/insertion from $LiCoO_2$ Cathode. *Electrochimica Acta* **2013**, *108*, 343–349. https://doi.org/10.1016/j.electacta.2013.06.120.

(41) Casas-Cabanas, M.; Rodríguez-Carvajal, J.; Canales-Vázquez, J.; Laligant, Y.; Lacorre, P.; Palacín, M. R. Microstructural Characterisation of Battery Materials Using Powder Diffraction Data: DIFFaX, FAULTS and SH-FullProf Approaches. *J. Power Sources* **2007**, *174* (2), 414–420. https://doi.org/10.1016/j.jpowsour.2007.06.216.

(42) Duffiet, M.; Blangero, M.; Cabelguen, P.-E.; Delmas, C.; Carlier, D. Influence of the Initial Li/Co Ratio in $LiCoO_2$ on the High-Voltage Phase-Transitions Mechanisms. *J. Phys. Chem. Lett.* **2018**, *9* (18), 5334–5338. https://doi.org/10.1021/acs.jpclett.8b02252.

(43) Godillot, G.; Huo, H.; Ménétrier, M.; Bourgeois, L.; Guerlou-Demourgues, L.; Delmas, C. Promising Nanometric Spinel Cobalt Oxides for Electrochemical Energy Storage: Investigation of Li and H Environments by NMR. *J. Phys. Chem. C* **2012**, *116* (50), 26598–26607. https://doi.org/10.1021/jp307458z.

(44) Gaudon, M.; Apheceixborde, A.; Ménétrier, M.; Le Nestour, A.; Demourgues, A. Synthesis Temperature Effect on the Structural Features and Optical Absorption of $Zn_{1-x}Co_xAl_2O_4$ Oxides. *Inorg. Chem.* **2009**, *48* (19), 9085–9091. https://doi.org/10.1021/ic900482v.

(45) Zhang, J.-N.; Li, Q.; Wang, Y.; Zheng, J.; Yu, X.; Li, H. Dynamic Evolution of Cathode Electrolyte Interphase (CEI) on High Voltage $LiCoO_2$ Cathode and Its Interaction with Li Anode. *Energy Storage Mater.* **2018**, *14*, 1–7. https://doi.org/10.1016/j.ensm.2018.02.016.

(46) Dahéron, L.; Dedryvère, R.; Martinez, H.; Flahaut, D.; Ménétrier, M.; Delmas, C.; Gonbeau, D. Possible Explanation for the Efficiency of Al-Based Coatings on $LiCoO_2$: Surface Properties of $LiCo_{1-x}Al_xO_2$ Solid Solution. *Chem. Mater.* **2009**, *21* (23), 5607–5616. https://doi.org/10.1021/cm901972e.

(47) Wang, H.; Jang, Y.-I.; Huang, B.; Sadoway, D. R.; Chiang, Y.-M. Electron Microscopic Characterization of Electrochemically Cycled $LiCoO_2$ and $Li(Al,Co)O_2$ Battery Cathodes. *J. Power Sources* **1999**, *81–82*, 594–598. https://doi.org/10.1016/S0378-7753(99)00108-1.

TOC Graphic

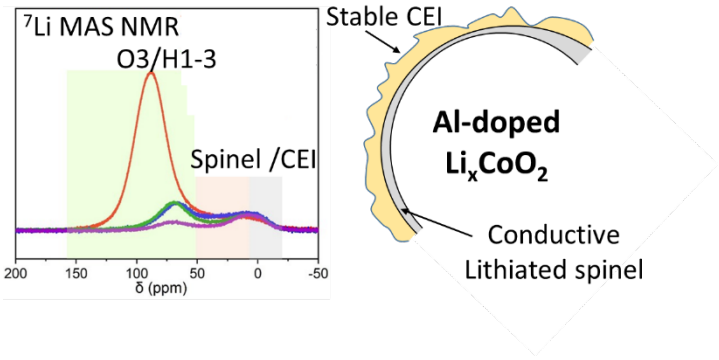
^{7}Li MAS NMR
O3/H1-3
Spinel /CEI
200
150
100
50
0
-50
δ (ppm)
Stable CEI
Al-doped
Li_xCoO_2
Conductive
Lithiated spinel